TGF-β by HIV-infected PBMC has been proposed to cause T cell functional defects that may be due to PCD (*28*). In addition, functional defects in antigen-presenting cells in HIV-infected men (*2*) may result in inadequate T cell activation that induces refractoriness to stimulation and PCD on subsequent activation. Groux *et al.* (*29*), by means of vital dye exclusion, observed activation-induced cell death of $CD4^+$ cells from HIV-infected individuals, after the cells had been cultured for 48 hours. Spontaneous cell death was not observed, and cell death after stimulation involved only $CD4^+$ cells, which might have resulted from their use of stimuli that preferentially activated $CD4^+$ cells.

We demonstrate that on culturing as well as after polyclonal activation, both $CD4^+$ and $CD8^+$ cells from HIV-infected individuals die as a result of apoptosis. In HIV infection in vivo, exposure to HIV proteins or disturbance of cytokine regulatory networks may cause a continuous, PCD-mediated depletion of T cells. Gradual deletion of immune regulatory T cells by PCD, in addition to the direct effects of highly cytopathic HIV variants (*30*, *31*), may contribute to the attenuation and collapse of the immune system.

REFERENCES AND NOTES

1. M. Clerici *et al.*, *J. Clin. Invest.* **84**, 1892 (1989).
2. F. Miedema *et al.*, *ibid.* **82**, 1908 (1988).
3. C. J. M. Van Noesel *et al.*, *ibid.* **86**, 293 (1990).
4. R. A. Gruters *et al.*, *Eur. J. Immunol.* **20**, 1039 (1990).
5. F. Miedema, M. Tersmette, R. A. W. Van Lier, *Immunol. Today* **11**, 293 (1990).
6. S. M. Schnittman *et al.*, *Science* **245**, 305 (1989).
7. S. M. Schnittman *et al.*, *Proc. Natl. Acad. Sci. U.S.A.* **87**, 6058 (1990).
8. R. A. Gruters *et al.*, *AIDS* **5**, 837 (1991).
9. R. H. Schwartz, *Science* **248**, 1349 (1990).
10. D. P. Stites *et al.*, *Clin. Immunol. Immunopathol.* **52**, 96 (1989).
11. J. F. Salazar-Gonzalez *et al.*, *J. Immunol.* **135**, 1778 (1985).
12. G. Pantaleo, S. Koenig, M. Baseler, H. C. Lane, A. S. Fauci, *ibid.* **144**, 1696 (1990).
13. H. E. Prince and E. R. Jensen, *Cell. Immunol.* **134**, 276 (1991).
14. E. Duvall and A. H. Wyllie, *Immunol. Today* **7**, 115 (1986).
15. C. A. Smith, G. T. Williams, R. Kingston, E. J. Jenkinson, J. J. T. Owen, *Nature* **337**, 181 (1989).
16. E. Martz and D. M. Howell, *Immunol. Today* **10**, 79 (1989).
17. A. H. Wyllie, R. G. Morris, A. L. Smith, D. Dunlop, *J. Pathol.* **142**, 67 (1984).
18. D. Cefai *et al.*, *J. Clin. Invest.* **86**, 2117 (1990).
19. J. C. Ameisen and A. Capron, *Immunol. Today* **12**, 102 (1991).
20. M. K. Newell, L. J. Haughn, C. R. Maroun, M. H. Julius, *Nature* **347**, 286 (1990).
21. A. H. Wyllie, J. F. K. Kerr, A. R. Currie, *Int. Rev. Cytol.* **68**, 251 (1980).
22. F. De Wolf *et al.*, *Br. Med. J.* **295**, 569 (1987).
23. L. Meyaard *et al.*, unpublished observations.
24. R. C. Duke, R. Chervenak, J. J. Cohen, *Proc. Natl. Acad. Sci. U.S.A.* **80**, 6361 (1983).
25. R. R. Jonker *et al.*, in preparation. Cells (0.5×10^6 to 2×10^6) were fixed in 1% formaldehyde and ethanol. After washing, cells were incubated (90 min, 15°C) in a total volume of 10 μl, with 55 μM biotin-labeled *d*-uridine 5′-triphosphate (UTP), a mixture of 19 μM *d*-adenosine 5′-triphosphate (ATP), *d*-guanosine 5′-triphosphate (GTP), and *d*-cytosine 5′-triphosphate (CTP), and DNA polymerase (100 U/ml) in 50 mM tris Cl (pH 7.8), 5 mM $MgCl_2$, 10 mM 2-mercaptoethanol, and bovine serum albumin (10 μg/ml). Cells were washed in phosphate-buffered saline (PBS) containing 0.1% (v/v) Triton X-100 and incubated with 40 μl of avidin-fluorescein isothiocyanate (2.5 μg/ml) and RNase (20 μg/ml) in 4× standard saline citrate (SSC), 0.1% (v/v) Triton X-100, and 5% (w/v) nonfat dry milk for 30 min at room temperature. Cells were then washed and resuspended in PBS containing 0.1% (v/v) Triton X-100 and propidium iodide (5 μg/ml) and analyzed on a FACSCAN cytofluorometer. The percentage of FITC-positive cells in G0/G1 phase as determined by propidium iodide staining represents the percentage of cells in apoptosis.
26. Z. F. Rosenberg and A. S. Fauci, *Immunol. Today* **11**, 176 (1990).
27. D. S. Schmid, J. P. Tite, N. H. Ruddle, *Proc. Natl. Acad. Sci. U.S.A.* **83**, 1881 (1986).
28. J. Kekow *et al.*, *J. Clin. Invest.* **87**, 1010 (1991).
29. H. Groux *et al.*, *J. Exp. Med.* **175**, 331 (1992).
30. M. Tersmette *et al.*, *Lancet* i, 983 (1989).
31. M. Tersmette *et al.*, *J. Virol.* **63**, 2118 (1989).
32. R. A. W. Van Lier *et al.*, *J. Immunol.* **139**, 2873 (1987).
33. K. S. Sellins and J. J. Cohen, *ibid.*, p. 3199. The cells were lysed with 0.5 ml of hypotonic lysis buffer (10 mM tris, 1 mM EDTA, 0.2% Triton X-100). The lysates were immediately centrifuged at 13,000*g* for 10 min, and the supernatant, containing fragmented DNA, was collected. Proteins were removed by phenol-chloroform-isoamylalcohol extraction and DNA was precipitated overnight with 1/20 volume of 3 M sodium acetate and 2 volumes of 96% ethanol at −20°C. Pellets were washed with 70% ethanol, air-dried and dissolved in 12 μl of RNase A (final concentration of 20 μg/ml) in 10 mM tris, 1 mM EDTA (pH 7.4), and incubated for 30 min at 37°C. After the addition of 3 μl of loading buffer [50 mM EDTA, pH 8.0, 15% (w/v) Ficoll, 0.25% (w/v) Bromophenol blue], samples were heated at 65°C for 15 min and electrophoresis was performed in 1.5% agarose for 1.5 hour at 60 V. DNA was visualized by staining with ethidium bromide under ultraviolet light.
34. R. De Jong, M. Brouwer, F. Miedema, R. A. W. Van Lier, *J. Immunol.* **146**, 2088 (1991).

35. We thank R. Fouchier (Central Laboratory of the Netherlands Red Cross Blood Transfusion Service), H. Janssen and J. Calafat (Netherlands Cancer Institute) for technical advice, and R. Van Lier and H. Schuitemaker for discussions and for reading the manuscript. Supported by a grant from the Dutch Ministry of Public Health. F.M. is a senior fellow of the Royal Netherlands Academy of Arts and Sciences.

14 November 1991; accepted 5 May 1992

Matrix-Mediated Synthesis of Nanocrystalline γ-Fe_2O_3: A New Optically Transparent Magnetic Material

Ronald F. Ziolo,* Emmanuel P. Giannelis,* Bernard A. Weinstein, Michael P. O'Horo, Bishwanath N. Ganguly, Vivek Mehrotra, Michael W. Russell, Donald R. Huffman

A new magnetic material with appreciable optical transmission in the visible region at room temperature has been isolated as a γ-Fe_2O_3/polymer nanocomposite. The synthesis is carried out in an ion-exchange resin at 60°C. Magnetization and susceptibility data demonstrate loading-dependent saturation moments as high as 46 electromagnetic units per gram and superparamagnetism for lower loadings where particle sizes are less than 100 angstroms. Optical absorption studies show that the small-particle form of γ-Fe_2O_3 is considerably more transparent to visible light than the single-crystal form. The difference in absorption ranges from nearly an order of magnitude in the "red" spectral region to a factor of 3 at 5400 angstroms. The magnetization of the nanocomposite is greater by more than an order of magnitude than those of the strongest room-temperature transparent magnets, $FeBO_3$ and FeF_3.

The design and synthesis of materials with nanometer dimensions, so called mesoscopic materials, are the subjects of intense current research. Materials with particles in the range 10 to 100 Å exhibit novel electronic, optical, magnetic, and chemical properties due to their extremely small dimensions (*1*). Although several studies have been devoted to the synthesis of nanometer-sized compound semiconductors, relatively little work exists for magnetic materials of similar dimensions (*2–8*). Potential applications for the latter exist in information storage (*9*, *10*), color imaging (*11*), bioprocessing (*12*), magnetic refrigeration (*13*), and ferrofluids (*14*). Such materials may also serve as models for small magnetic particles, which may comprise a portion of interstellar dust (*15*).

A critical obstacle in assembling and

R. F. Ziolo, M. P. O'Horo, B. N. Ganguly, Xerox Webster Research Center, Xerox Corporation, Webster, NY 14580.
E. P. Giannelis, V. Mehrotra, M. W. Russell, Department of Materials Science and Engineering, Cornell University, Ithaca, NY 14853.
B. A. Weinstein, Department of Physics, State University of New York at Buffalo, Buffalo, NY 14260.
D. R. Huffman, Department of Physics, University of Arizona, Tucson, AZ 85721.

*To whom correspondence should be addressed.

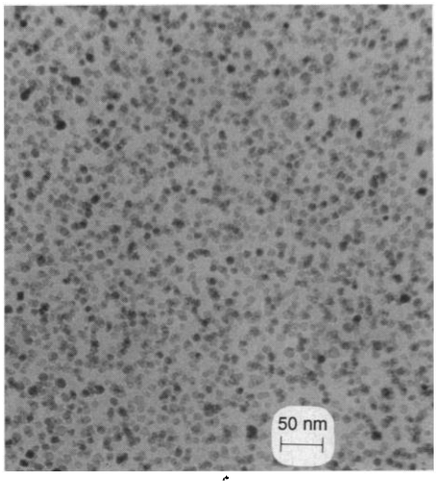

Fig. 1. Bright-field transmission electron micrograph of a microtomed section of composite containing 21.8% γ-Fe_2O_3 by weight in an 8% cross-linked polystyrene resin. The iron oxide particles range in size from 50 to 100 Å.

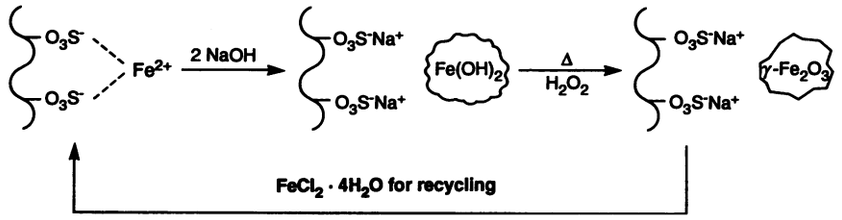

Fig. 2. Schematic of the γ-Fe_2O_3 precipitation process using Fe(II) in an ion-exchange resin.

maintaining a nanoscale material from molecular clusters is the tendency of the latter to aggregate to reduce the energy associated with the high ratio of surface area to volume. By use of a polymer matrix in the form of a synthetic ion-exchange resin, we have been able to stabilize, isolate, and characterize a mesoscopic form of γ-Fe_2O_3 that, unlike most magnetic materials at room temperature, has an appreciable degree of optical transparency in the visible region (*16*).

The polymer matrix used in this study is a commercial ion-exchange resin manufactured by Dow Chemical Company and marketed under the trade name Dowex. It is composed of sulfonated polystyrene, which is cross-linked with divinylbenzene to form a three-dimensional, porous polymer network. The dry resin has a nominal cation-exchange capacity of 5.2 meq/g. In general, 8% or less cross-linked resin was used in the form of spherical beads having diameters of 30 to 150 μm.

The resin was exchanged with Fe(II) or Fe(III) from an aqueous solution of the respective chloride, followed by thorough washings to remove excess physisorbed Fe ions. Elemental analyses of the resins after washing showed the expected Fe:S atom ratios of 1:2 or 1:3, respectively, confirming complete ion exchange. In the case of the Fe(II) resin, exposure to a 12.5 N solution of NaOH caused a rapid change in color to green followed by a gradual change to deep red-black on exposure to air. Heating to 60°C followed by the dropwise addition of a dilute aqueous H_2O_2 solution accelerated the conversion to oxide. In the case of Fe(III), an aqueous suspension of the resin was heated and maintained at 60°C during the dropwise addition of N_2H_4 with stirring. Aqueous NaOH was added afterward to bring the pH to 13 to 14. After stirring for several hours, both resins were thoroughly washed with water to neutral pH and dried. Elemental analyses of the resins showed typical Fe contents of 9.8 and 7.8%, respectively, with no change in the Fe:S atom ratio, indicating no Fe loss during preparation. The ion-exchange capability of the resin remained intact after the above treatments, and resins containing more Fe can be made by recycling the composite through the above preparative procedures. The Fe contents of ten-cycle, 4% cross-linked resins, for example, were typically 42 and 37%, respectively.

The oxide phase was identified as γ-Fe_2O_3 (maghemite) by conventional and synchrotron energy-dispersive x-ray powder diffraction methods and Mössbauer spectroscopy. This assignment was consistent with the subsequent magnetization, optical, and electron diffraction data for the material. Transmission electron microscope (TEM) analyses of numerous samples, prepared from both procedures and with different loadings, show a relatively uniform, high-density distribution of oxide in the polymer matrix (*17a*). The maghemite particles constitute the only crystalline phase present and are spherical or cubic in shape. Furthermore, the particles are relatively uniform in size throughout the matrix and from sample to sample, within the limits of cross-link density and site sulfonation homogeneity in the polymer. It was further observed by TEM analysis that multiple loadings of Fe served initially to increase the number density of particles in the polymer matrix rather than their size (*17b*). A typical cross section of the composite is shown in Fig. 1. The sample is a two-cycle Fe(III) resin containing 21.8% γ-Fe_2O_3 by weight. The particles range in size from 50 to 100 Å and are morphologically indistinguishable with respect to size and shape from those of the one- and three-cycle resins. The TEM analyses of numerous samples of the Fe(II) and Fe(III) processed resins show little deviation from this morphology, which may be considered characteristic of the γ-Fe_2O_3 composite (*17a*, *17b*, *18*). In both the Fe(II) and Fe(III) cases, the nanoscale particle size was in accord with the Bragg peak broadening observed in the x-ray diffraction patterns.

To a first approximation, the formation of γ-Fe_2O_3 in the ion-exchange resin may be represented schematically as in Fig. 2 for Fe(II). Here, the Fe attaches to the resin as the hydrated $Fe(H_2O)_6^{2+}$ species and in the presence of base forms the emerald-green $Fe(OH)_2$, which is detected spectroscopically. Although $Fe(OH)_2$ dissolves in concentrated NaOH to form species such as $Fe(OH)_6^{4-}$, it is gelatinous in lower concentrations and may form a localized nucleation site for the formation of γ-Fe_2O_3. The conversion of $Fe(OH)_2$ to γ-Fe_2O_3 is accelerated by heating and may take place through intermediates such as FeO(OH) and Fe_3O_4 (*19*). Regardless of the mechanism for the formation of γ-Fe_2O_3 in the polymer, and subsequent composite, it is apparent that the matrix favors the formation of the gamma phase for both the Fe(II) and Fe(III) procedures. Identical reactions carried out in the absence of the polymer matrix resulted in nonmagnetic amorphous or poorly crystalline aggregates of other oxide phases with dimensions in the micrometer range. In the case of Fe(II), precipitation in the absence of the polymer network under equivalent conditions resulted in a mixture of phases of hexagonal α- and β-$FeO(OH)_3$. When the polymer matrix was loaded with Fe(II) in excess of its ion-exchange capacity and treated, δ-FeO(OH) formed on the external surfaces of the γ-Fe_2O_3–loaded beads.

The above data underscore the critical role played by the polymer matrix in the formation of the nanometer composite. The matrix not only provides spatially localized sites for nucleation but also minimizes the degree of aggregation of the iron oxide particles and imposes an upper limit on their size, as evidenced by the sample to sample reproducibility and the initial increase in particle number density rather than size with multiple loadings. In addition, the matrix-mediated synthesis of γ-Fe_2O_3 takes place at or near room temperature, whereas other methods require temperatures in excess of 150°C (*20*). Furthermore, the present matrix synthesis, under the conditions described, favors the formation of equiaxial particles in the shape of cubes with rounded corners. This morphology is relatively uncommon for γ-Fe_2O_3 (*19*).

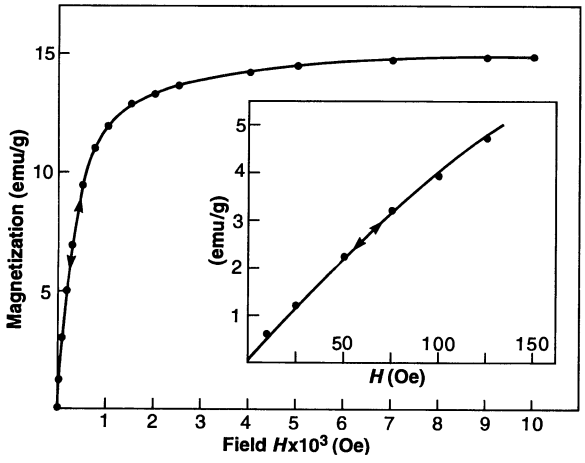

Fig. 3. Room-temperature magnetization curve to 10 kG for the γ-Fe_2O_3 composite shown in Fig. 1. (Inset) A 2- by 40-fold expansion of the initial portion of the magnetization curve showing the absence of hysteresis.

In bulk, γ-Fe_2O_3 is a spinel type ferrimagnet with a Néel temperature well above 600°C (*20*). As the particles become smaller, a critical size is reached at which the bulk magnetic characteristics of retentivity and coercivity vanish. Such particles are called superparamagnetic and are in a state in which thermal fluctuations supersede the Weiss anisotropy (*21*). We obtained field- and temperature-dependent magnetization data for the composites using a vibrating sample magnetometer. A typical magnetization curve as a function of field at room temperature is shown in Fig. 3. The initial susceptibility shows no hysteresis at room temperature, that is, both the retentivity and coercivity are zero, consistent with superparamagnetic behavior and the nanoscale dimensions of the particles. At 10 kG, the composite has a magnetic saturation moment of 15 emu/g. The elemental analysis of the composite shows 15.28% Fe, which suggests a 21.8% by weight loading of γ-Fe_2O_3, consistent with the exchange capacity of the resin and the two-cycle loading of Fe. The calculated saturation moment for this loading of γ-Fe_2O_3, based on the bulk value (*22*) of 76.0 emu/g at 20°C, is 16.6 emu/g. The difference, which is 10% or less for the samples measured, is presumed to be due to small particle magnetic effects (*19*, *22*). The highest saturation moment so far observed for the composite is 46 emu/g; this occurred in a ten-cycle Fe(II) resin displaying hysteresis and containing particles 250 Å on edge (*17*).

Measurements of dc magnetic susceptibility, determined by the Faraday method as a function of temperature and magnetic field, also confirmed the superparamagnetic behavior of the nanocomposites. The room-temperature susceptibility at 2 kG for an Fe(II) resin containing 2% γ-Fe_2O_3 by weight was 6×10^{-4} emu/g. A TEM analysis of the sample showed a Gaussian distribution of particles with a mean size of 85 ± 20 Å. Temperature-dependent susceptibility data for the sample showed a blocking temperature of 58 K (*23*). Field-dependent magnetization data for the sample below 50 K showed expected hysteresis, which vanished at higher temperatures. Magnetization data at 10 K are illustrated in Fig. 4, A and B, for the field-cooled and zero–field-cooled cases, respectively. It is evident from the figures that these curves are superimposable, suggesting that the particles are magnetically single-phased. The observed coercivity (~1 kOe) is approximately that expected for a system of randomly oriented equiaxial particles with cubic magnetocrystalline anisotropy (*24*).

Throughout the course of our work it became apparent that the magnetic composite, when compared to other magnetic materials, showed a disproportionately larger degree of optical transparency in the visible region than its magnetic strength would suggest. This was particularly evident in comparison to bulk γ-Fe_2O_3. In order to quantify this observation, we measured the optical absorption characteristics of the nanocomposite and of single-crystal γ-Fe_2O_3. Optical data for the latter were previously unavailable.

The optical absorption of the composite, in the form of spherical beads 45 ± 1 μm in diameter, was investigated over the range 4500 to 7500 Å. Use of an optical microprobe for the absorption measurements allowed us to minimize lensing effects in the beads and to obtain an estimate of the refractive index for subsequent correction of the absorption spectra against reflection losses. The former was accomplished by inserting field stops that limit the effective aperture under parallel illumination to a region 5 to 7 μm at the center of a bead. The latter required use of the microprobe's calibrated depth-measurement scale to determine the focal length, from which the refractive index was obtained according to the standard thick lens expressions (*25*). This method yielded an average index of $n = 1.6 \pm 0.1$ for the 21.8% by weight loaded beads. A similar value for n was obtained by microscopical liquid immersion techniques and application of the Becke test (*26*).

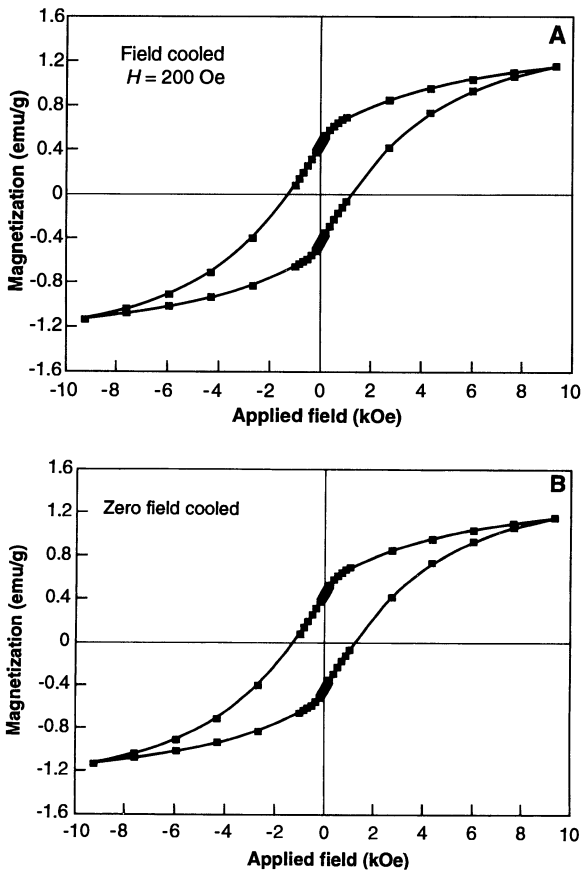

Fig. 4. (**A**) Field-cooled magnetization curve at 10 K and 200 Oe for an Fe(II) resin containing 85 Å γ-Fe_2O_3 at 2% by weight. (**B**) Zero–field-cooled curve at 10 K for the same sample.

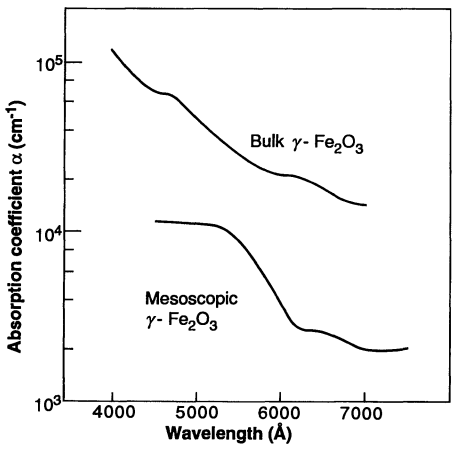

Fig. 5. Room-temperature optical absorption spectra of mesoscopic and single-crystal γ-Fe_2O_3. The former derives from the sample described in Fig. 1.

The reference sample of γ-Fe_2O_3 consists of a single-crystal γ-Fe_2O_3 thin-film epitaxially grown on an MgO substrate (*27*). Absorption spectra were recorded on a Cary 5 spectrophotometer. The sample thickness, determined by measuring the Fe (0.68 keV) x-ray escape depth, was 0.3 μm. The refractive index of the film was taken to be that of hematite (*28*), $n \sim 3.0$.

Figure 5 compares the average absorption spectrum of the mesoscopic form of γ-Fe_2O_3, obtained from the optical density data of the composite, to that of the single-crystal form of γ-Fe_2O_3. The optical density data for the composite were obtained as an average over four different specimens exhibiting sample-to-sample absorption variations of ±10% within the measured wavelength region. We extracted the absorption coefficient of the mesoscopic form of the oxide from the optical density data of the composite by treating the beads as free-standing films of thickness equal to their diameter scaled by the volume loading fraction, 0.052 (*29*), and assuming a uniform distribution of iron oxide throughout the bead. The standard thick film analysis was then applied (*30*). This approximation was premised on the small acceptance aperture of the microprobe, which observes only ~0.25 radian of arc. At the same level of approximation, the reflectivity corrections for each of the spectra in Fig. 5 are based on the real part of the refractive index in the transparent regime (the above n values). Because the reflectivities are ~0.1, the errors introduced are not large. We estimate for both spectra that the overall uncertainty throughout the visible region does not exceed ±30%, the largest contribution being due to increased scattered light in the beads below 5000 Å.

Two important results are evident in Fig. 5. First, the mesoscopic form of γ-Fe_2O_3 is considerably more transparent to visible light than the single-crystal form. The difference in absorption between the two forms ranges from nearly an order of magnitude in the "red" spectral region to a factor of 3 at 5400 Å. In fact, the absorption coefficient of the mesoscopic γ-Fe_2O_3 remains below 10^4 cm^{-1} throughout much of the visible.

The second important feature in Fig. 5 is the wavelength difference between the main absorption edges in the mesoscopic and bulk spectra, with the mesoscopic γ-Fe_2O_3 edge "red-shifted" by 300 to 600 Å. This is a relatively large shift corresponding to 0.15 to 0.30 eV (~5 to 10% of the edge energy) and is indicative of strong interactions affecting the small-particle form of γ-Fe_2O_3.

The low absorption of the mesoscopic γ-Fe_2O_3, compared to the single-crystal form, indicates a strongly reduced oscillator strength. There are many ways in which this could occur, including effects due to the high surface to volume ratio of the γ-Fe_2O_3 particles, cation impurities and vacancy distribution in the γ-Fe_2O_3, and chemical interactions with the matrix. At present, none of the effects can be ruled out. However, such a reduced oscillator strength in the presence of superparamagnetism has been predicted for similar nanoscale magnetic systems as a consequence of intrinsic correlation effects (*31*). Essentially, it is argued that the reduction in oscillator strength arises because confinement within dimensions of a few hundred angstroms can inhibit exchange coupling. On the other hand, the red shift of the absorption edge measured in the composite beads argues against the importance of quantum confinement, because an increase in optical energies would then be expected on the basis of standard single-particle effective-mass theory (*32*). The competition between single particle and correlation effects in mesoscopic systems is a subject of much current interest (*33*). Recent theoretical work on GaAs "quantum dots" indicates that electron correlations can begin to become important for dimensions ≧100 Å (*34*). In γ-Fe_2O_3, single particle effects could be minimized by a particularly large band-edge effective mass. We believe that the present absorption results may indicate the importance of appreciable electron correlation interactions in the mesoscopic γ-Fe_2O_3 (*35*).

At room temperature, most magnetic materials are optically opaque. The only materials that have a spontaneous magnetic moment at room temperature and are transparent well into the visible (absorption coefficient ≦40 cm^{-1}) are $FeBO_3$ and FeF_3. Both are weak ferromagnets at room temperature with impractically low magnetizations of ~3 and 1 emu/g, respectively (*36*). Other transparent ferromagnets, such as K_2CrCl_4 and EuSe, for example, have appreciable magnetizations, but only near absolute zero (*37*). The present composites offer a compromise between these extremes and, although not ferromagnetic, possess practical levels of magnetization at room temperature with enhanced transparency in the visible that is similar to that of yttrium iron garnet (*38*, *39*). This unique combination of properties is a consequence of the nanometer dimensions of the matrix-stabilized iron oxide.

REFERENCES AND NOTES

1. See, for example, L. E. Brus *et al.*, *J. Mater. Res.* **4**, 704 (1989).
2. H. Okata *et al.*, *Chem. Mater.* **2**, 89 (1990).
3. S. Mann and J. P. Hannington, *J. Colloid Interface Sci.* **122**, 326 (1988).
4. X. K. Zhao, P. J. Herve, J. H. Fendler, *J. Phys. Chem.* **93**, 908 (1989).
5. V. Papaefthymiou *et al.*, *J. Appl. Phys.* **67**, 4487 (1990).
6. R. D. Shull *et al.*, *ibid.*, p. 4490.
7. _____, *Mater. Res. Soc. Symp. Proc.* **206**, 455 (1991).
8. B. J. Tarasevich and P. C. Rieke, *ibid.* **174**, 51 (1990).
9. L. Gunther, *Phys. World* **3**, 28 (December, 1990).
10. R. G. L. Audran and A P. Huguenard, U.S. Patent 4,302,523 (1981).
11. R. F. Ziolo, U S Patent 4,474,866 (1984).
12. L. Nixon, C. A. Koval, R. D. Noble, G. S. Slaff, *Chem. Mater.* **4**, 117 (1992); R. H. Marchessault, S. Ricard, P. Rioux, *Carbohydrate Res.* **224**, 133 (1992).
13. R. D McMichael, R. D. Shull, L. J. Swartzendruber, L. H. Bennett, R E. Watson, *J. Magn. Magn. Mater.* **111**, 29 (1992).
14. I. Anton *et al.*, *ibid.* **85**, 219 (1990).
15. D. R. Huffman, *Adv. Phys.* **26**, 129 (1977).
16. Part of this work appeared in the form of abstracts. R. F Ziolo, W. H. H Günther, M. P. O'Horo, APS Conference Proceedings (American Physical Society, New York, 1978), no. 40, p. 409; R. F. Ziolo, W. H. H. Gunther, M. P. O'Horo, R. Kellerman, B. Ganguly, 175th American Chemical Society National Meeting, Anaheim, CA, 13 to 17 March 1978, J K. Vassiliou, V. Mehrotra, M. W. Russell, E. P. Giannelis, Materials Research Society Meeting, Boston, MA, 26 to 30 November 1990.

17a. Cross-sectional analyses of fully loaded beads show a higher concentration of particles in the outer portion of the beads relative to that in the bulk

17b. At higher oxide loadings, particle size may increase with additional loadings rather than number. A TEM analysis of the ten-cycle Fe(II) resin, for example, showed cubic particles 250 Å on edge. Presumbaly, this can occur when the particle population distorts the resin matrix enough to critically alter the nucleation site geometry and associated diffusional and chemical kinetics. Under the reported synthesis conditions, the effect seems to be more pronounced in the Fe(II) process than in the Fe(III) process. In subsequent loadings, the number of accessible nucleation sites may also diminish.

18. Resin source, reaction temperature and time, and cross-link density influence the particle size, which in some cases can be controlled at approximately 25 to 50, 25 to 100, and 75 to 250 Å. Under some conditions, acicular particles or mixtures of acicular and spherical particles may form.
19. D. J. Craik, Ed., *Magnetic Oxides* (Wiley, New York, 1975), part 2, pp. 697–708.
20. A. H. Morrish, in *Crystals· Growth, Properties, and Applications*, H. C Freyhardt, Mgr. Ed. (Springer-Verlag, New York, 1980), vol. 2, pp. 171–197.

21. C. P. Bean and J. D. Livingston, *J. Appl. Phys.* **30**, 120s (1959).
22. B. D. Cullity, *Introduction to Magnetic Materials* (Addison-Wesley, Reading, MA, 1972), pp. 201 and 383–441.
23. J. K. Vassiliou, V. Mehrotra, M. W. Russell, E. P. Giannelis, *Mater. Res. Soc. Symp. Proc.* **206**, 561 (1991). If we take 58 K as the blocking temperature and assume that the particles are spherical with an average diameter of 85 Å, we calculate a magnetic anisotropy of 6.2×10^5 erg/cm^3. The critical radius for superparamagnetic γ-Fe_2O_3 particles at room temperature is 385 Å, corresponding to a magnetic anisotropy of 0.04×10^5 erg/cm^3. The large deviation from the value calculated for the 85 Å particles is probably due to the surface anisotropy resulting from the small particle size and possibly the presence of some Fe^{2+} ions in the structure of the oxide. Similar arguments have been used to explain the difference in magnetic anisotropy (three orders of magnitude) calculated from blocking temperature data for 100 Å NiO particles.
24. E. Kneller, in *Magnetism and Metallurgy*, A. E. Berkowitz and E. Kneller, Eds. (Academic Press, New York, 1969), vol. 1, chap. 8.
25. A. F. Jenkins and H. White, *Fundamentals of Optics* (McGraw-Hill, New York, ed. 4, 1976), p. 84.
26. W. C. McCrone and J. G. Delly, *The Particle Atlas* (Ann Arbor Science, Ann Arbor, MI, ed. 2, 1973), vol. 1, p. 72.
27. H. Takei and S. Chiba, *J. Phy. Soc. Jpn.* **21**, 1255 (1966).
28. G. V. Samaonov, Ed., *The Oxide Handbook* (Plenum, New York, 1973), p. 334. The complete optical characterization of this film is in progress.
29. This value was derived from the iron oxide weight loading, assuming a density of 5.07 g/cm^3 for γ-Fe_2O_3 and 1.0 g/cm^3 for the polymer.
30. C. J. Tauc, in *Progress in Semiconductors*, A. F. Gibson and R. E. Burgess, Eds. (Temple Press, London, 1965), vol. 9.
31. B. N. Ganguly, *Proc. IEEE Indust. Appl. Soc.* (Annual meeting, 1 to 5 October 1978, Toronto, Ontario, Canada), p. 251
32. D. K. Smith and C. Mailhiot, *Rev. Mod. Phys.* **62**, 173 (1990).
33. U. Merkt and Ch. Sikorski, *Semicond. Sci. Technol.* **5**, S182 (1990).
34. G. W. Bryant, *Phys. Rev. Lett.* **59**, 1140 (1987).
35. R. F. Ziolo *et al.*, in preparation.
36. R. Wolfe, A. J. Kurtzig, R. C. LeCraw, *J. Appl. Phys.* **41**, 1218 (1970).
37. P. Day, *Acc. Chem. Res.* **12**, 236 (1979).
38. G. B. Scott, D. E. Lacklison, J. L. Page, *Phys. Rev. B.* **10**, 971 (1974).
39. The Faraday and magnetic circular dichroism spectra of the γ-Fe_2O_3 nanocomposite have been measured in the visible and near-ultraviolet (R. F. Ziolo *et al.*, in preparation).
40. The Cornell University contribution was sponsored in part by the National Science Foundation (DMR-88188558) through the Materials Science Center. E.P.G. and B.A.W. acknowledge grants from Xerox Webster Research Center. We thank R. J. Gruber for support and encouragement. M.W.R. was supported under an IBM Fellowship administered through the Cornell Ceramics Program. We thank H. Takei and S. Chiba for supplying the reference sample of γ-Fe_2O_3. We thank R. D. Shull and R. D. McMichael (low-temperature magnetization data), R. G. Fernquist (γ-Fe_2O_3 thickness measurement), T. P. Debies (x-ray photoelectron spectroscopy), A. Orzechowski (optical microscopy), K. Kemp (scanning electron microscopy), J. A. Czerniawski (TEM), K. Johnson (TEM), R. H. Herber (Mössbauer spectroscopy), W. H. H. Günther, F. J. DiSalvo, J. W. Otto, and J. K. Vassiliou for their contributions. The Cornell High Energy Synchrotron Source facility is supported by a grant from the National Science Foundation.

23 April 1992; accepted 14 May 1992

The Chemistry of Bulk Hydrogen: Reaction of Hydrogen Embedded in Nickel with Adsorbed CH_3

A. D. Johnson, S. P. Daley, A. L. Utz, S. T. Ceyer*

Studies in heterogeneous catalysis have long speculated on or have provided indirect evidence for the role of hydrogen embedded in the catalyst bulk as a primary reactant. This report describes experiments carried out under single-collision conditions that document the distinctive reactivity of hydrogen embedded in the bulk of the metal catalyst. Specifically, the bulk H atom is shown to be the reactive species in the hydrogenation of CH_3 adsorbed on Ni(111) to form CH_4, while the H atoms bound to the surface were unreactive. These results unambiguously demonstrate the importance of bulk species to heterogeneous catalytic chemistry.

Forty years ago, several studies (*1–3*) noted a correlation between the hydrogenation activity of a Raney nickel catalyst and the hydrogen content in the catalyst, but the exact role of the hydrogen, whether it be a reactant or a modifier of the electronic structure and hence of the activity of the nickel, remains unclear (*4–6*). The reason for the dearth of information about these practically and commercially important hydrogenation reactions is the inability to carry them out under single-collision conditions, such as afforded by ultrahigh vacuum (UHV) surface science techniques, where microscopic reaction steps are discernable. Specifically, it is the inability to produce the bulk hydrogen at low H_2 pressures ($<10^{-4}$ torr) that precludes these reactions from being studied. The kinetic limitations imposed by high barriers (*7*) to dissociative absorption of H_2 into nickel metal and into many other transition metal catalysts necessitate high hydrogen pressures. However, we have recently demonstrated two methods of synthesizing bulk hydrogen in Ni under low-pressure UHV conditions (*8, 9*) and a method to detect it spectroscopically (*9*). In this report, we document the chemistry of this bulk hydrogen. We find that a bulk H atom has a reactivity that is distinct from that of a H atom adsorbed on a surface. In particular, a bulk H atom is the reactive species in the hydrogenation of CH_3 adsorbed on Ni(111) to form methane. Hydrogen atoms bound to the surface are unreactive with the CH_3 species. Analogous results are obtained for the D isotope as a bulk or an adsorbed species.

The experiment is carried out in a UHV chamber that is equipped for surface analysis and is precisely coupled to a supersonic molecular beam source. The experimental procedures are similar to our previous studies (*10–12*). In the experiment described here, bulk D is synthesized by exposure of the Ni(111) crystal at 130 K to atomic D as described previously (*8, 9*). The bulk D is characterized by a vibrational mode at 575 cm^{-1}, as measured by high-resolution electron energy loss spectroscopy (HREELS), and recombines and desorbs as D_2 between 180 and 220 K. Exposure to atomic D not only results in D embedded within the Ni lattice but also in a monolayer (ML) of deuterium adsorbed on the surface. The surface-bound D is a problem because it blocks sites necessary for the second reactant, adsorbed CH_3, that we synthesize by the dissociative chemisorption of CH_4 (*13*). Therefore, the D adsorbed on the surface must be removed. The removal of the surface-bound deuterium cannot be effected thermally because it is more stable than bulk D, recombining and desorbing between 320 and 390 K. Therefore, a nonthermal mechanism for removal of the surface-bound D is necessary.

We have recently observed such a mechanism, collision-induced recombinative desorption (*14*). In this process, a beam of energetic Xe atoms impinges on the deuterium-covered Ni(111) surface at glancing incident angles. The impacts of the collisions momentarily jostle the lattice, causing the adsorbed D atoms to recombine and desorb as D_2. We used this technique in our synthesis to sweep the deuterium off the surface, leaving the deuterium in the bulk unperturbed. Its efficacy for the H isotope is demonstrated by the HREEL spectra in Fig. 1. Figure 1A shows the vibrational spectrum of the Ni(111) crystal saturated with the H isotope so that the equivalent coverage of H in the bulk is 1.5 ML and the surface coverage is 1 ML. The symmetric and antisymmetric vibrational stretch modes for the surface-bound H are visible at 1170 and 955 cm^{-1}, respectively, and the threefold degenerate vibrational mode for H bound in an octahedral interstitial site is visible at 790 cm^{-1} (*9*). After exposure to 9×10^{17} Xe atoms incident at 40° from the normal angle with 144 kcal mol^{-1} of energy (Fig. 1B), the surface mode at 1170 cm^{-1} is

Department of Chemistry, Massachusetts Institute of Technology, Cambridge, MA 02139.

*To whom correspondence should be addressed.